Nonlinear Dyn (2020) 99:1923–1935
https://doi.org/10.1007/s11071-019-05435-2

ORIGINAL PAPER

Dynamical response of a pendulum driven horizontally by a DC motor with a slider–crank mechanism

Grzegorz Litak · Arkadiusz Syta · Grzegorz Wasilewski · Grzegorz Kudra · Jan Awrejcewicz

Received: 19 May 2019 / Accepted: 15 December 2019 / Published online: 1 January 2020

Abstract The pendulum is excited horizontally by a system of a DC motor and a slider–crank mechanism. Mathematical modeling is realistic and based on experimental rig, taking into account details concerning friction in the joints as well as realistic mass distribution in particular elements of the system. Using basic nonlinear tools as phase portraits, Poincaré maps, and Fourier spectra, we report various solutions including periodic, quasi-periodic and non-periodic ones. To identify chaotic solutions, we used the 0–1 test. The simulation results were qualitatively confirmed by experiments.

Keywords DC-driven pendulum · Nonlinear dynamics · Chaos identification

G. Litak (✉)· A. Syta
Faculty of Mechanical Engineering, Lublin University of Technology, Nadbystrzycka 36, 20-618 Lublin, Poland
e-mail: g.litak@pollub.pl

A. Syta
e-mail: a.syta@pollub.pl

G. Wasilewski · G. Kudra · J. Awrejcewicz
Department of Automation, Biomechanics and Mechatronics, Lodz University of Technology, Stefanowskiego 1/15, 90-924 Łódź, Poland
e-mail: grzegorz.wasilewski@lodz.pl

G. Kudra
e-mail: grzegorz.kudra@p.lodz.pl

J. Awrejcewicz
e-mail: jan.awrejcewicz@p.lodz.pl

1 Introduction

Pendulum or systems of pendulums in different configurations play a role of paradigmatic model to investigate different problems of physics including especially nonlinear dynamics as well as wide spectrum of engineering systems. Even single harmonically excited pendulum can exhibit almost all phenomena of classical nonlinear dynamics, including classical bifurcations, swinging oscillatory and rotational motion, chaotic solutions and multistability. Single pendulum is a subject of continuous interests of scientists and their numerical, experimental and analytical studies of this system [1–3]. There exist books devoted to the pendulum, e.g., in the monograph [4] one can find a comprehensive study of the subject including the historical point of view. The more recent example is the book [5]. Single externally forced pendulum cannot model many physical and engineering systems and cannot exhibit some nonlinear dynamics phenomena. This is a reason of investigations of other mechanical systems based on the pendulum, e.g., parametric pendulum [6–8], multi-pendulum systems [9,10] or systems of pendulums with control [11]. Moreover parametric pendulum systems are often used as energy harvesters. See, for example, experimental investigations of a rotating parametric tri-pendulum system [12], or numerical and experimental analysis of an inclined parametrically excited pendulum [13], as a wave energy converters.

Apart from the classic case of a pendulum with harmonic vertical or horizontal parametric excitation, it is often analyzed a pendulum with suspension point driven with a slider–crank mechanism. For example, modeling and analysis of bifurcation dynamics of such single pendulum are presented in the works: [14–17]—for horizontal driving and [18,19]—for vertical motion of the pendulum pivot. In those works mainly basic numerical analysis of bifurcation dynamics is presented. Some of the investigated models assume kinematic driving in the form of a given rotational motion of the crank as a known function of time [18], or additional mathematical model of DC motor driving the crank is taken into account [14–17,19]. In the first case, the difference between the pendulum driven by the crank–shaft mechanism and classic case of the pendulum with harmonic parametric forcing lies in different characteristics of motion of the pendulum's pivot point. Moreover in the works [15–17], the model is based on experimental rig and simulation results fit the experimental data.

Dynamical systems consisting of a DC motor and a pendulum is a topic of many recent studies [14–17,19–22]. The work [21] is a comprehensive review of mechanical systems with limited energy sources, consisting of, but not limited to, pendulum systems. Here the main idea is to provide a limited power source to the pendulum resonator. Similar systems can be also used for vibration energy harvesting [8,19]. Such a system is excited by periodic manner with some of the sub-/super-harmonics contributions and can move in various swinging or/and rotational modes. For systems composed of an unbalanced electric DC motor placed on a flexible support, this system can show the Sommerfeld effect [20,22].

This study is a continuation of the works [15–17]. Full mathematical model of electromechanical experimental rig consisting of the pendulum forced by through a system of a DC motor and a slider–crank mechanism was built and the parameters were estimated leading to good agreement between the simulation and experimental results [15]. But for constant input voltage the rotational speed of the DC motor was in good approximation constant and relatively good results were obtained by the model assuming constant rotational speed of the crank [16]. Then the experimental rig was modified, i.e., the DC motor was replaced by the one of lower power, so the effect of significant influence of the mechanical system dynamics on rotational speed of DC motor was achieved, making the dynamics of the system more rich. The new full model of the electromechanical system was identified and verified based on preliminary examples of bifurcation dynamics obtained both numerically and experimentally [17].

In the present paper we focus on analysis of numerical solutions of model from the last work. Using the standard Poincaré maps and Fourier spectra, we identify the chaotic solutions. The corresponding bifurcation diagrams show the regions of periodic and chaotic solutions which are verified by the 0–1 test. Simulation results correspond to dynamic behavior of real electromechanical system. One of novel elements of the present work is realistic modeling of the pendulum driven by a DC motor through slider–crank mechanism, in fairly good agreement with the experimental results. Consequently, the suggested 0–1 test for chaos detection allows simultaneous investigations of experimental and numerical signals. It is noteworthy to remind that the 0–1 test is a stochastic tool for chaos detection from an scalar response of the dynamical system [23]. Especially, neglecting the phase space reconstruction is very useful for experimental signals.

The present work is organized as follows. In Sect. 2, the experimental rig (Sect. 2.1), mathematical models of mechanical system (Sect. 2.2) and DC motor (Sect. 2.3) and final mathematical model of full electromechanical system (Sect. 2.4) are presented. In Sect. 3, the process of the parameters' estimation is described. Section 4 is devoted to numerical analysis of the system dynamics and model validation. Preliminary numerical simulations are presented in Sect. 4.1, while Sect. 4.2 exhibits results of further analysis based on the 0–1 test applied to both the numerical and experimental series. The is paper closed by Sect. 5 with some concluding remarks.

2 Experimental rig and mathematical model

2.1 Experimental rig

Figure 1a, b exhibits experimental rig of the investigated system. Mechanical system consists of a rotational disk 1, a connecting rod 2, a slider 3 and a pendulum 4. The slider moves along a guide 5. A DC motor with gearbox 6 drives the disk. Shaft of the disk is mounted on a support 7. Position of the system is measured by the encoders, and the data are collected by

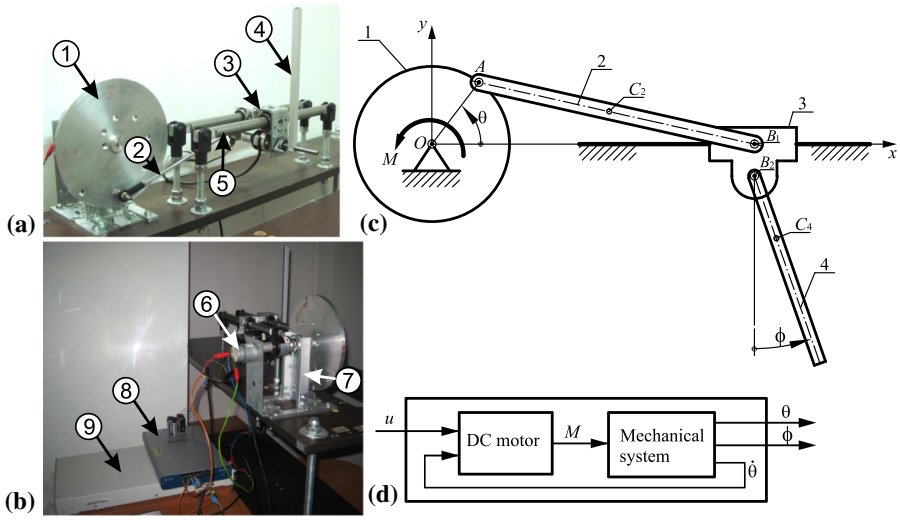

Fig. 1 Experimental rig (**a**, **b**), physical model of the mechanical system (**c**) and block diagram of electromechanical system (**d**)

data acquisition device 8. DC motor is supplied by a voltage generator 9. More technical information about experimental rig one can find in the work [17].

2.2 Mechanical system

Physical concept of the mechanical part of experimental rig is presented in Fig. 1c. It is planar two-degree-of-freedom mechanical system consisting of four rigid bodies: rotational disk 1, connecting rod 2, slider 3 and pendulum 4. They are connected by the use of four rotational joints denoted by O, A, B_1 and B_2. Position of the system is described by two generalized coordinates: θ − angular position of disk 1 and ϕ −angular position of the pendulum 4. The disk 1 represents all rotating masses of the DC motor, gear transmission and real disk of the experimental setup reduced to the coordinate θ while M stands for the corresponding equivalent torque generated by the motor.

Based on Lagrange's formalism, the following form of the governing equations has been found

$$\mathbf{M}(\mathbf{q})\ddot{\mathbf{q}} + \mathbf{N}(\mathbf{q})\dot{\mathbf{q}}^2 + \mathbf{w}(\mathbf{q}) + \mathbf{r}(\mathbf{q}, \dot{\mathbf{q}}) = \mathbf{f}(t) \tag{1}$$

where

$$\mathbf{M}(\mathbf{q}) = \begin{bmatrix} m_{11} & m_{12} \\ m_{21} & m_{22} \end{bmatrix}, \mathbf{N}(\mathbf{q}) = \begin{bmatrix} n_{11} & n_{12} \\ n_{21} & 0 \end{bmatrix},$$
$$\mathbf{w}(\mathbf{q}) = \begin{bmatrix} \frac{a}{b}(b - b_1)m_b g \cos\theta \\ mgr \sin\theta \end{bmatrix},$$
$$\mathbf{r}(\mathbf{q}, \dot{\mathbf{q}}) = \begin{bmatrix} M_{R\theta}(\theta, \dot{\theta}) \\ M_{R\phi}(\dot{\phi}) \end{bmatrix}, \mathbf{f}(t) = \begin{bmatrix} M(t) \\ 0 \end{bmatrix},$$
$$\mathbf{q} = \begin{bmatrix} \theta \\ \phi \end{bmatrix}, \dot{\mathbf{q}} = \begin{bmatrix} \dot{\theta} \\ \dot{\phi} \end{bmatrix}, \ddot{\mathbf{q}} = \begin{bmatrix} \ddot{\theta} \\ \ddot{\phi} \end{bmatrix}, \dot{\mathbf{q}}^2 = \begin{bmatrix} \dot{\theta}^2 \\ \dot{\phi}^2 \end{bmatrix},$$

and where the following notation has been used

$$\begin{aligned}
m_{11} &= I_O + a^2\left(F^2(m + m_s) + F_1^2 m_b\right) \\
&\quad + \frac{a^2}{b^2}\cos^2\theta\left((b - b_1)^2 m_b + G^2 I_b\right), \\
m_{12} &= m_{21} = -amrF\cos\phi, \\
m_{22} &= I + mr^2, \\
n_{11} &= aFH\left(1 + \frac{m_s}{m}\right) + aF_1H_1 \\
&\quad - \frac{a^2}{2b^2}\sin 2\theta\left((b - b_1)^2 m_b\right. \\
&\quad \left. + G^2 I_b\left(1 - \frac{a^2}{b^2}\cos^2\theta\right)\right), \\
n_{12} &= amrF\sin\phi, \\
n_{21} &= -rH\cos\phi,
\end{aligned} \tag{2}$$

while

$$\begin{aligned}
G &= \frac{1}{\sqrt{1 - \frac{a^2}{b^2}\sin^2\theta}}, \\
F &= \left(1 + \tfrac{a}{b}G\cos\theta\right)\sin\theta, \\
F_1 &= \left(1 + \tfrac{ab_1}{b^2}G\cos\theta\right)\sin\theta, \\
H &= am\left(\cos\theta + \tfrac{a}{b}G\cos 2\theta + \tfrac{1}{4}\tfrac{a^3}{b^3}G^3\sin^2 2\theta\right), \\
H_1 &= am_b\left(\cos\theta + \tfrac{ab_1}{b^2}G\cos 2\theta + \tfrac{1}{4}\tfrac{a^3 b_1}{b^4}G^3\sin^2 2\theta\right).
\end{aligned} \tag{3}$$

In Eqs. (1–3) m_b, m_S and m denote masses of the subsequent links (2, 3 and 4); I_O, I_b and I—mass moments of inertia of the bodies 1, 2 and 4, respectively, with respect to their mass centers denoted by the points O, C_2 and C_4; $a = OA$, $b = AB_1$, $b_1 = AC_2$ and $r = B_2C_4$—the corresponding lengths of the mechanical system; $M_{R\theta}$ and $M_{R\phi}$—the corresponding generalized forces representing resistance forces in the system.

The resistance forces reduced to the corresponding generalized coordinates read

$$\begin{aligned} M_{R\theta}\left(\theta,\dot{\theta}\right) &= c_O\dot{\theta} + \frac{2}{\pi}M_O \arctan\left(\varepsilon_O\dot{\theta}\right) \\ &+ a^2F^2c_s\dot{\theta} + \frac{2}{\pi}aFT_s \arctan\left(\varepsilon_s aF\dot{\theta}\right), \\ M_{R\phi}(\dot{\phi}) &= c_B\dot{\phi} + \frac{2}{\pi}M_B \arctan\left(\varepsilon_B\dot{\phi}\right). \end{aligned} \tag{4}$$

where c_O, c_s and c_B are viscous damping coefficients in rotational joint O, slider and rotational joint B_2, respectively. The parameters M_O, T_s and M_B stand for the corresponding magnitudes of friction torques or force in nonlinear parts of resistance models: $\frac{2}{\pi}M_O \arctan(\varepsilon_O\dot{\theta})$ (in the joint O), $\frac{2}{\pi}T_s \arctan(\varepsilon_s\dot{x}_B)$ (in the slider) and $\frac{2}{\pi}M_B \arctan(\varepsilon_B\dot{\phi})$ (in the joint B), where ε_O, ε_s and ε_B are additional parameters and $\dot{x}_B = -aF\dot{\theta}$ is velocity of the point B_1 (velocity of the slider 3). Since for $\varepsilon_O, \varepsilon_s, \varepsilon_B \to \infty$, the corresponding elements of the resistance models tend to sign functions, for relatively large value of these parameters one obtains Coulomb friction models with magnitudes of friction force or torque independent from loading. On the other hand, it occurs (see works [15,17]) that the smaller values of these parameters allow for better fitting of the model to the experimental data. Here we use set of parameters with the quantities ε_s and ε_B obtained as a result of estimation. The parameter ε_O is not identified, and it is assumed to be equal to 10^3, since angular velocity $\dot{\theta}$ does not change the sign and its variability is relatively small when compared to other velocities in the system, so we expect that influence of this parameter on system dynamics is smaller than the corresponding impact of the parameters ε_s and ε_B. The model does not posses elements related directly to resistance in the rotational joints A and B_1. Equivalent influence of friction in these joints on the system dynamics can, however, appear in particular elements of models of resistance in the joint O and between the slider and the guide.

2.3 DC motor

The relationship between voltage, current and rotational speed for the armature-controlled DC motor takes the following form

$$u = L\frac{\mathrm{d}i}{\mathrm{d}t} + Ri + K_E\frac{\mathrm{d}\theta_0}{\mathrm{d}t}, \tag{5}$$

where u—the input voltage, i—winding current, $\mathrm{d}\theta_0/\mathrm{d}t$—angular velocity of the motor shaft (before the gear transmission), L—inductance, R—armature resistance, and K_E—the proportionality coefficient between rotational speed of the DC motor and the back electromotive force.

Taking into account that $M_0 = K_T i$, $i_g = \dot{\theta}_0/\dot{\theta} = M/M_0$, where M_0—the torque generated on the motor shaft (before the gear transmission), K_T—the corresponding parameter, i_g—the gear transmission ratio, and neglecting the inductance $L = 0$, one gets the following algebraic expression for the torque M acting on the disk 1 as a function of the input voltage u

$$M = \frac{K_T}{R}i_g u - \frac{K_E K_T}{R}i_g^2\frac{\mathrm{d}\theta}{\mathrm{d}t}. \tag{6}$$

Assumption of inductance equal to zero in the mathematical model of DC motor results from our expectation that electrical time constant L/R is small enough not to have a significant impact on the dynamics of the entire mechanical system. Further results of identification and model verification confirm the validity of this assumption.

2.4 Final model of electromechanical system

Taking into account the relation (6), one can present the governing equations of motion (1) in the following way

$$\mathbf{M}(\mathbf{q})\ddot{\mathbf{q}} + \mathbf{N}(\mathbf{q})\dot{\mathbf{q}}^2 + \mathbf{w}(\mathbf{q}) + \mathbf{r}_e(\mathbf{q},\dot{\mathbf{q}}) = \mathbf{f}_e(t), \tag{7}$$

where the modified resistance and external forces' vectors take the following form

$$\mathbf{r}_e(\mathbf{q},\dot{\mathbf{q}}) = \begin{bmatrix} (C_O + a^2F^2c_s)\dot{\theta} + \frac{2}{\pi}M_O \arctan(\varepsilon_O\dot{\theta}) + \frac{2}{\pi}aFT_s \arctan(\varepsilon_s aF\dot{\theta}) \\ c_B\dot{\phi} + \frac{2}{\pi}M_B \arctan(\varepsilon_B\dot{\phi}) \end{bmatrix},$$

$$\mathbf{f}_e(t) = \begin{bmatrix} K_M u(t) \\ 0 \end{bmatrix},$$

where the following parameters have been defined

$$K_M = \frac{K_T}{R} i_g, \quad C_O = \frac{K_E K_T}{R} i_g^2 + c_O.$$

Note that the back electromotive force (multiplied by some constant parameters) has been moved to the vector of resistance forces and gathered with the equivalent viscous damping in the rotational joint O. Final equations (7) describe a system composed of mechanical pendulum and DC motor with mutual interactions between them. The pendulum acts on rotational speed, back electromotive force and torque of the DC motor, which drives the pendulum.

3 Parameters' estimation

In the parameters' estimation process (for more information see works [15,17]), we define and minimize the following objective function

$$F_O(\mathbf{p}) = \frac{\sum_{i=1}^{N} \int_{\theta_0}^{\theta_{fi}} \left[w_\phi (\phi_{si}(\theta,\mathbf{p}) - \phi_{ei}(\theta,\mathbf{p}))^2 + w_\omega \left(\omega_{fsi}(\theta,\mathbf{p}) - \omega_{fei}(\theta,\mathbf{p})\right)^2 \right] \mathrm{d}\theta}{\sum_{i=1}^{N} (\theta_{fi} - \theta_0)}, \tag{8}$$

where $\mathbf{p}$—vector of the estimated parameters; N—number of the compared pairs of solutions; ϕ_{si}, ϕ_{ei}—the i-th pair of the simulated and experimental angular position ϕ of the pendulum; ω_{fsi}, ω_{fei}—the i-th pair of the simulated and experimental filtered angular velocity of the disk 1; θ_0—initial angular position of the disk 1 common for all the compared solutions, θ_{fi}—final angular position of the disk 1 in the i-th pair of the compared solutions, w_ϕ and w_ω—the corresponding weights.

The experimental rig is equipped with encoders allowing for direct measurement of angular positions of disk 1 and pendulum 4. In order to obtain a smooth signal which can play a role of experimental angular velocity of the disk 1, we pass its experimental angular position $\theta_{ei}(t)$ (obtained via linear interpolation of the experimental data) through a filter of transfer function $G_f(s) = \frac{s}{(T_f s+1)^2}$. As an output one obtains the signal $\omega_{fei}(t)$. In order to have the proper numerical signal, comparable with its experimental counterpart, the simulated angular position $\theta_{si}(t)$ of the disk 1 is also passed through the same filter, where the output is $\omega_{fsi}(t)$.

Note that the signals in the objective function (8) are compared in the domain of the angular position θ of the disk 1. Since there is a lack of any common synchronizing signal (e.g., common periodic input) in experimental and numerical models, any uncertainties in the real system (e.g., small random fluctuations of friction in the joints) can lead to random changes in angular position of the disk, which cannot be predicted using deterministic mathematical model. These changes can become significant after some time (for longer time series) and may lead to some problems in fitting the simulation to the experimental data. This is the reason that we have changed the domain of the compared signals from time to the angle θ.

In the estimation process, we have used three experimental solutions, with the input voltage having the form of step function $u(t) = u_0\mathbf{1}(t)$, for $u_0 = -10.8$, -8.0, -6.5 V and common initial conditions for $t = 0$: $\theta_0 = -\pi/2$ rad/s, $\phi_0 = 0$ rad, $\dot{\theta}_0 = \dot{\phi}_0 = 0$ rad/s. The signals $\theta(t)$ and $\phi(t)$ were recorded on the time interval $[0, 60]$ s. The orbits tend to stable periodic solutions, thanks to which one avoids the problem of sensitivity to small perturbations.

Some of the parameters are relatively easy to be obtained via direct measurements of masses and lengths. They have been measured and assumed to be constant during the parameters' estimation process: $m_b = 0.057\,\mathrm{kg}$, $m_s = 0.777\,\mathrm{kg}$, $m = 0.226\,\mathrm{kg}$, $a = 0.080\,\mathrm{m}$ and $b = 0.300\,\mathrm{m}$. The remaining quantities assumed to be constant are: $\varepsilon_O = 10^3$ s/rad,

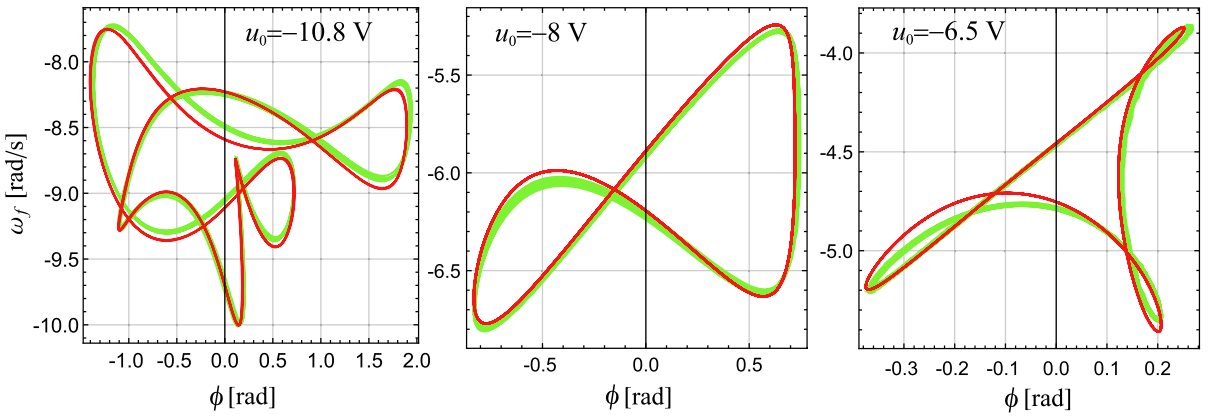

Fig. 2 Three numerical solutions (red lines) compared with the corresponding experimental data (green lines) for final fitting in the parameters' estimation process (here $f = \phi$ and $\omega_f = \dot{\phi}$). (Color figure online)

$g = 9.81\,\mathrm{m/s^2}$ and $T_f = 0.1$ s. It is also assumed that $w_\phi = 1\ \mathrm{rad}^{-2}$ and $w_\omega = 1\ \mathrm{s^2 rad^{-2}}$.

Other parameters (elements of the vector $\mathbf{p}$) are estimated based on minimization of the objective function $F_0(\mathbf{p})$: $K_M = 3.066 \times 10^{-2}\ \mathrm{N \cdot m/V}$, $C_O = 3.003 \times 10^{-2}\ \mathrm{N \cdot m \cdot s}$, $M_O = 1.937 \times 10^{-2}\ \mathrm{N \cdot m}$, $I_O = 5.252 \times 10^{-3}\ \mathrm{kg \cdot m^2}$, $I_b = 2.373 \times 10^{-6}\ \mathrm{kg \cdot m^2}$, $b_1 = 8.801 \times 10^{-2}\ \mathrm{m}$, $c_s = 2.171 \times 10^{-1}\ \mathrm{N \cdot s}$, $T_s = 6.583 \times 10^{-1}\ \mathrm{N}$, $I = 1.426 \times 10^{-3}\ \mathrm{kg \cdot m^2}$, $r = 5.417 \times 10^{-2}\ \mathrm{m}$, $c_B = 2.486 \times 10^{-4}\ \mathrm{N \cdot m \cdot s}$, $M_B = 2.162 \times 10^{-3}\ \mathrm{N \cdot m}$, $\varepsilon_s = 27.68$ s/m, $\varepsilon_B = 3.193$ s/rad. Figure 2 presents comparison of three simulated phase plots with the corresponding results based on the experimental data for final fitting in the parameters' estimation process.

The process of minimization of the objective function (8) (estimation of the parameters) is based on the Nelder–Mead method [24,25], a kind of downhill simplex method and commonly used optimization algorithm, implemented among others in MATLAB and Scilab environments in the form of function fminsearch. However, the function (8) is highly dimensional and nonlinear and can possess many local minima while we are looking for global one. Since fundamentally the Nelder–Mead method stops at local minima, it is well known the problem how to force the algorithm to seek for the global minimum. There exist different methods minimizing the problem of local minima, among others starting from different initial guesses or stopping the classical Nelder–Mead algorithm and then perturbing the solution and starting the minimization process again. In this work we mix the both mentioned ways. But it is always a problem how strong perturbation of the current solution should be. Here we use the concept of bootstrap restarting and the algorithm presented in the work [26].

If $F_O(\mathbf{p}, \mathbf{y})$ is an objective function for a given parameter vector $\mathbf{p}$ and experimental data $\mathbf{y}$, then the algorithm can be depicted as follows: 0) Using some starting vector $\mathbf{p}_0$, find a local minimum of function $F_O(\mathbf{p}, \mathbf{y})$: $\hat{\mathbf{p}}_0$. Then repeat the steps 1–3 for $k = 1, \ldots, K$. 1) Create a bootstrap resample $\mathbf{y}_k^*$ of original data $\mathbf{y}$. Using the starting vector $\hat{\mathbf{p}}_{k-1}$, find a local minimum of function $F_O(\mathbf{p}, \mathbf{y}_k^*)$: $\mathbf{p}_k^*$. 2) Using the starting vector $\mathbf{p}_k^*$, find a local minimum of function $F_O(\mathbf{p}, \mathbf{y})$: $\mathbf{p}_k$. 3) If $F_O(\mathbf{p}_k, \mathbf{y}) < F_O(\hat{\mathbf{p}}_{k-1}, \mathbf{y})$, then set $\hat{\mathbf{p}}_k := \mathbf{p}_k$, otherwise set $\hat{\mathbf{p}}_k := \hat{\mathbf{p}}_{k-1}$.

The bootstrap resample of the same size as the original data is obtained using random selection with replacements of 3 solutions from the original set of 3 experimental time series. In practice the local minimum is searched for until reaching an assumed tolerance or maximum number of iterations of the simplex method. In the steps 0 and 2 of the presented above algorithm, the maximum number of iterations is equal to 800, while in the step 1 the Nelder–Mead procedure is stopped after reaching 200 iterations. Moreover we have found it more practical to find firstly some initial solution using shorter experimental time series. Therefore, we have applied the depicted above algorithm using the experimental time series limited to the initial 5 s of motion (see Fig. 3a), and then, using the estimated parameters as initial guess, we have applied it to the full time series of 60 s (see Fig. 3b). Figure 3 presents value of the objective function versus number of bootstrap

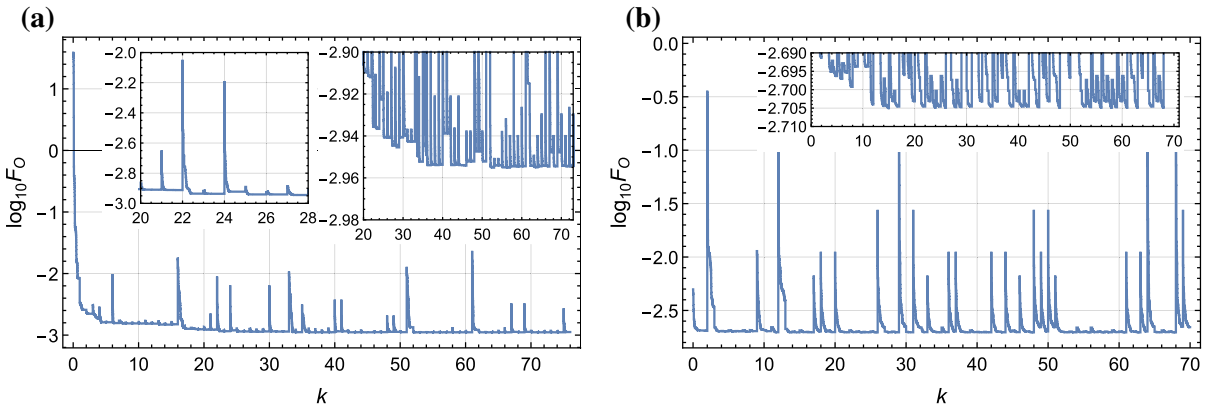

Fig. 3 Value of the objective function F_O versus number of bootstrap restarts k, in identification process based on initial parts of 5 s (**a**) and 60 s (**b**) of experimental solutions for $u_0 = -10.8, -8.0$ and -6.5 V

restarts k obtained during the steps 2 of the algorithm. It should be noted that it have not been proved that the presented solution is the global minimum of the defined objective function. We only know that we have mathematical model with the parameters which allows for reliable numerical simulations of good agreement with experimental data. The software for parameters' estimation and simulations presented in the present paper were developed in MATLAB environment and with the use of ODE45 (Dormand–Prince) solver.

4 Numerical simulations and model validation

4.1 Preliminary numerical simulations

We performed number of numerical simulation of the model for different values of the parameters. We noticed the sensitivity of the dynamics of the system due to changes in one of the parameters, in this case the value of parameter u_0 was changed, which is responsible for the initial supply voltage of the DC motor. Figure 4 presents comparison of the phase portraits with the Poincaré sections for chosen values of u_0 and the nodal initial conditions. Analyzing Fig. 4, you can see a noticeable difference in the dynamic response of the system with the increase in the value of u_0. One can notice vibrations with odd periods ($u_0 = -11.75$-period 5, $u_0 = -10.5$-period 3, $u_0 = \{-11.55, -8.25\}$-period 1, $u_0 = -9.75$-period 11) as well as even periods ($u_0 = -9.5$-period 4), as well as quasi-periodic ($u_0 = \{-11.25, -10.2\}$) and chaotic vibrations ($u_0 = -9.0$). Confirmation in a qualitative manner of the system's sensitivity to the value of u_0 can be done by means of spectral analysis. Figure 5 shows the power spectra for the single ϕ time series for the respective u_0 values. At a later stage, we wanted to confirm the results of the qualitative analysis in a quantitative manner by setting the values of the indicator that would distinguish between periodic and non-periodic solutions.

4.2 Test 0–1

We used, among other methods like the maximal Lyapunov exponent, the 0–1 test. This method developed by Gottwald and Melbourne [23,27,28] is based on the statistical and spectral properties of a single time series and can be used as a chaos indicator for both model and experimental systems [29,30]. Below we would like to briefly describe the method. In the first step, the considered one-dimensional time series is presented in two-dimensional space (p, q) by means of transformation:

$$p_c(n) = \sum_{j=1}^{n} x(j)\cos(jc),$$
$$q_c(n) = \sum_{j=1}^{n} x(j)\sin(jc), \tag{9}$$

where x is a time series and $c \in (0, \pi)$ constant corresponds to fixed frequency in Fourier decomposition of the time series x. In our case, as the input data for the 0–1 test we used the ϕ coordinate from the phase space. Exemplary phase portraits corresponding to the numerical solutions in Fig. 4 are shown in Fig. 6.

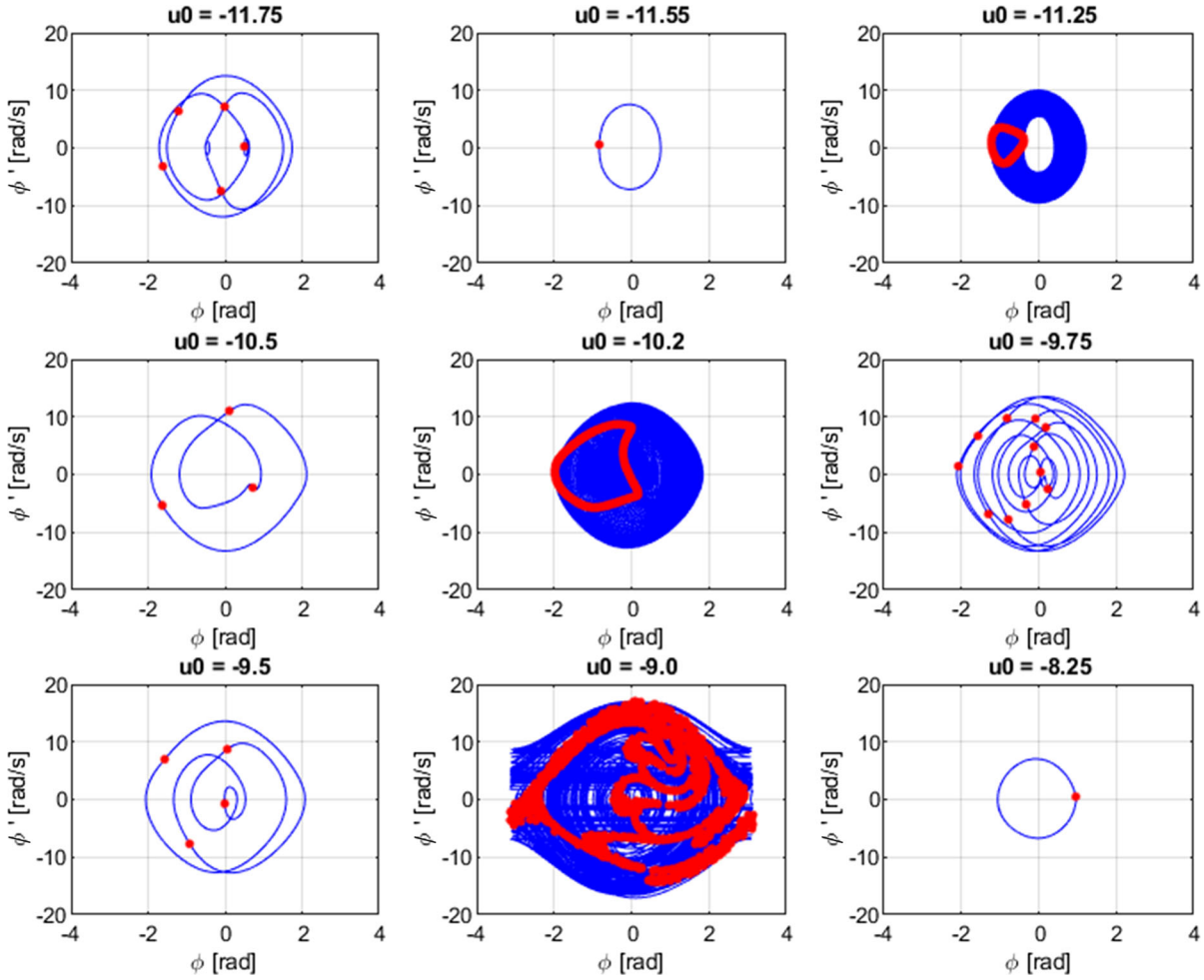

Fig. 4 Phase portraits with Poincaré sections of the system obtained numerically from the proposed model (Eq. 7) for different values of u_0

Comparing the figures for individual u_0 values, one can notice their circle like motion (characteristic for periodic vibrations) and similar to random walk (characteristic for non-periodic vibrations) only in case $u_0 = -9.0$. In the next step, we would like to measure the boundedness or unboundedness of the auxiliary trajectory in (p, q) plane by the asymptotic growth of the mean square displacement:

$$M_c(n) = \lim_{N\to\infty} \frac{1}{N} \sum_{j=1}^{N} [p_c(j+n) - p_c(j)]^2 + [q_c(j+n) - q_c(j)]^2 , \quad (10)$$

where n corresponds to total number of points (in practice the above limit is assumed by taking $n = n_{\max}$) and $n_{\max} << N$ (usually $N = n/10$). It turns out that the M_c is bounded in time in case x is a regular solution or scales linearly with time in case x is a non-regular solution. In the last step, the asymptotic growth of the M_c function is calculated as a final value (K_c):

$$K_c(n) = \lim_{n\to\infty} \frac{\log M_c(n)}{\log n}. \quad (11)$$

Alternatively, the correlation method can be used to determine the K_c value:

$$K_c(n) = \frac{\mathrm{cov(X, M_c)}}{\sqrt{\mathrm{var(X)var(M_c)}}}, \quad (12)$$

where $X = \{1, \ldots, n_{\max}\}, M_c = \{M_c(1), \ldots, M_c(n_{\max})\}$. The definitions of the covariance cov(X, Y) and vari-

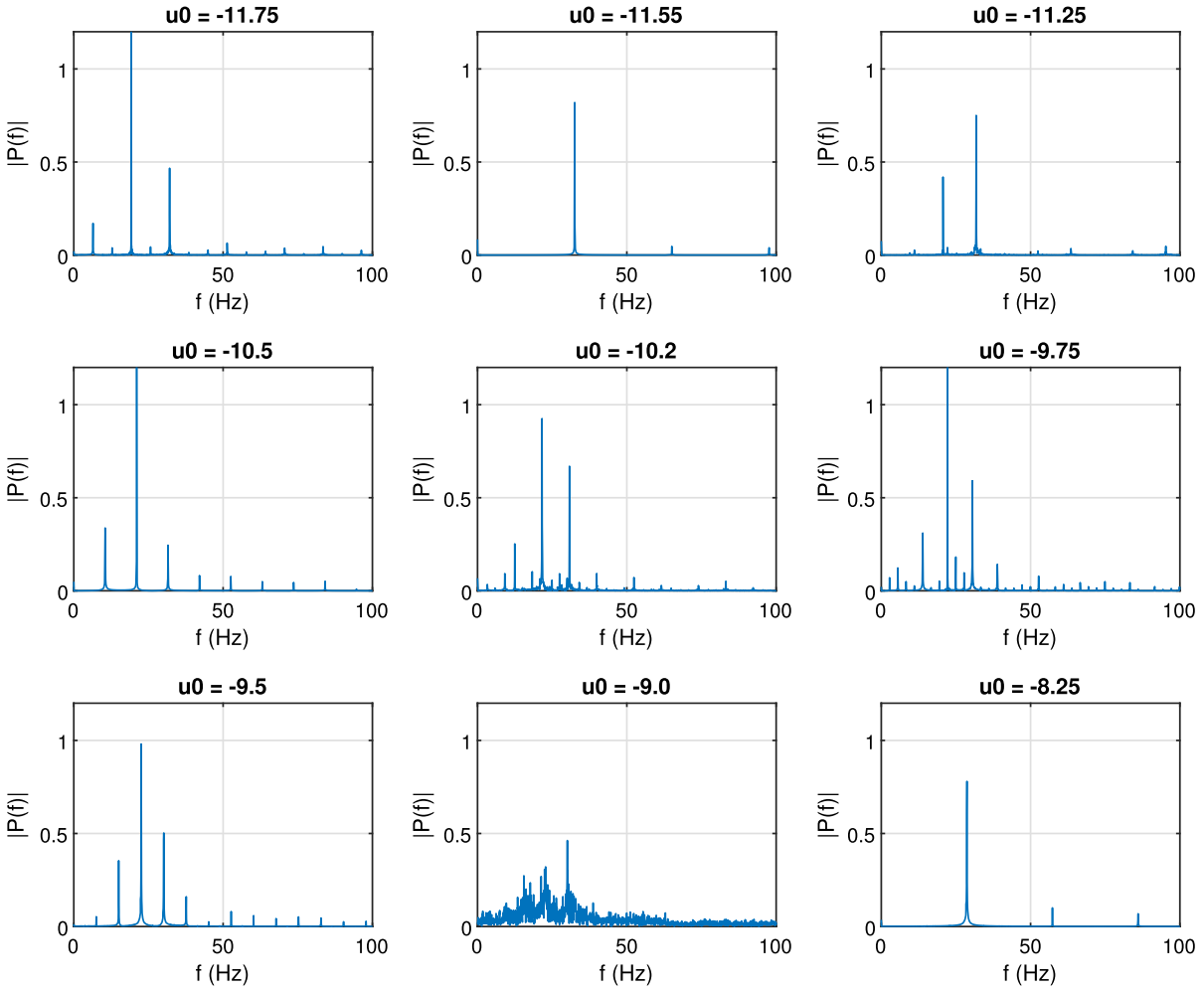

Fig. 5 Power spectra of the ϕ coordinate of the system sampled with 3.124 kHz frequency for the corresponding cases shown in Fig. 4

ance var(X) functions for arbitrary vectors X and Y of $n_{\max}$ elements, and the corresponding mean values $\hat{X}$ and $\hat{Y}$ are given by the formulas:

$$\mathrm{cov(X,Y)} = \frac{1}{\mathrm{n_{max}}} \sum_{\mathrm{n=1}}^{\mathrm{n_{max}}} (\mathrm{X(n)} - \hat{\mathrm{X}})(\mathrm{Y(n)} - \hat{\mathrm{Y}}),$$
$$\mathrm{var(X)} = \mathrm{cov(X,X)}. \tag{13}$$

It should be noted that in the case c is a resonance frequency proportional to the component of the Fourier transform of the x series, the transformation will lead to the Brownian motion regardless of the dynamics of the system. To avoid this, for the implementation of the method, many c values assumed (usually 100 is sufficient) and then calculated the median of all K_c values which is less sensitive to the extreme values then the mean. Defined function takes two values (in the limit): $K \approx 0$ for regular dynamic, or $K \approx 1$ for chaotic dynamic. Comparison of the 0–1 test for different values of u_0 is presented in Fig. 7.

Figure 7 shows clear difference in the dynamics response characteristics of the pendulum driven by a crank–shaft–slider mechanism and a DC motor. One can see that from one side, for regular: periodic and quasi-periodic motions ($u_0 \in (-12.0, -9.85) \cup (-9.5, -9.14) \cup (-8.37, -8)$ values of the $K \approx 0$. On the other side, for chaotic motion ($u_0 \in (-9.86, -9.51) \cup (-9.13, -8.38)$ values $K \approx 1$. In those regions, there are also some periodic solutions that are easily identified by the 0–1 test. To be more specific line structures visible in the bifur-

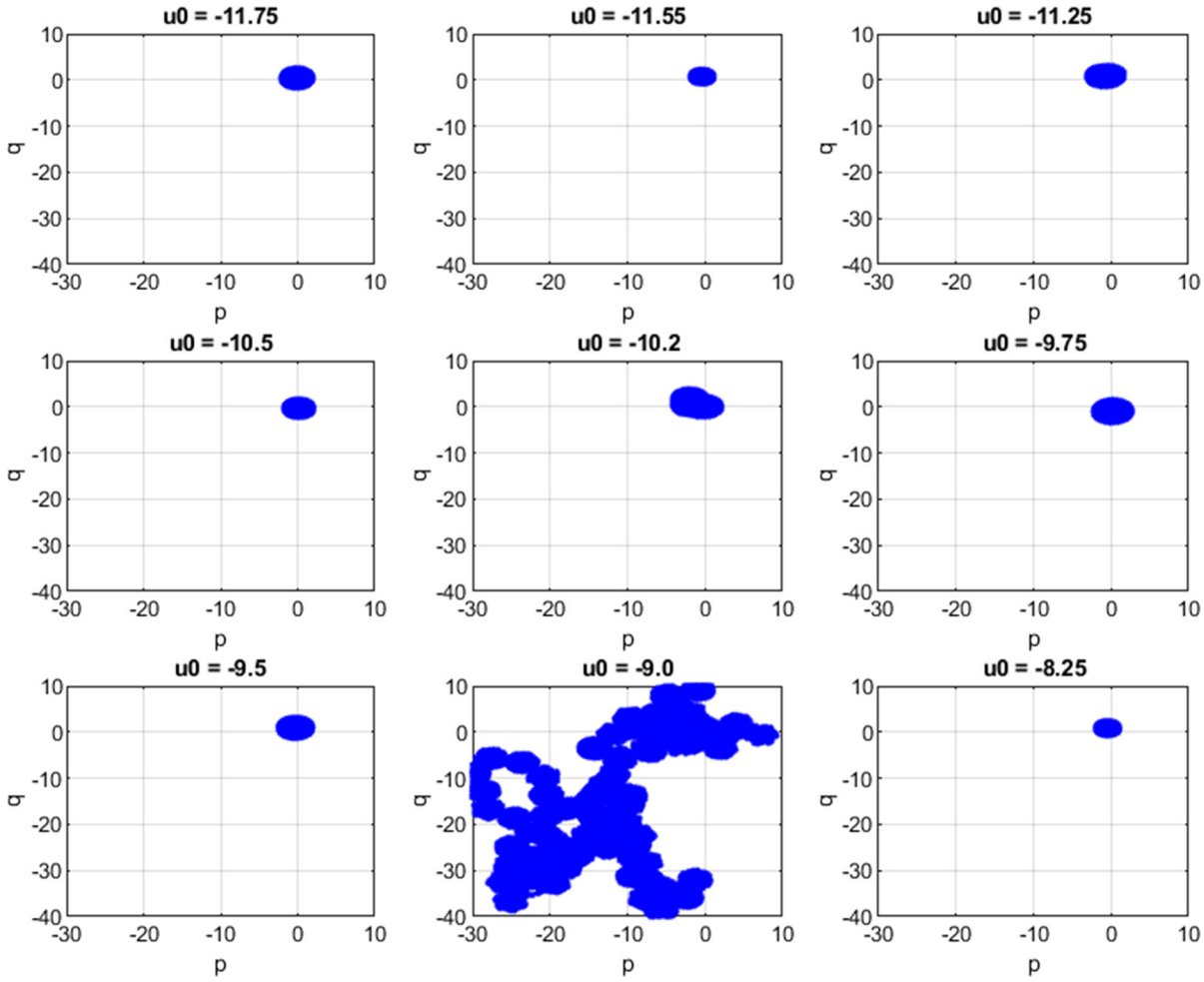

Fig. 6 Numerically simulated ϕ coordinate of the system in the space (p, q) for fixed $c_0 = 1.0$

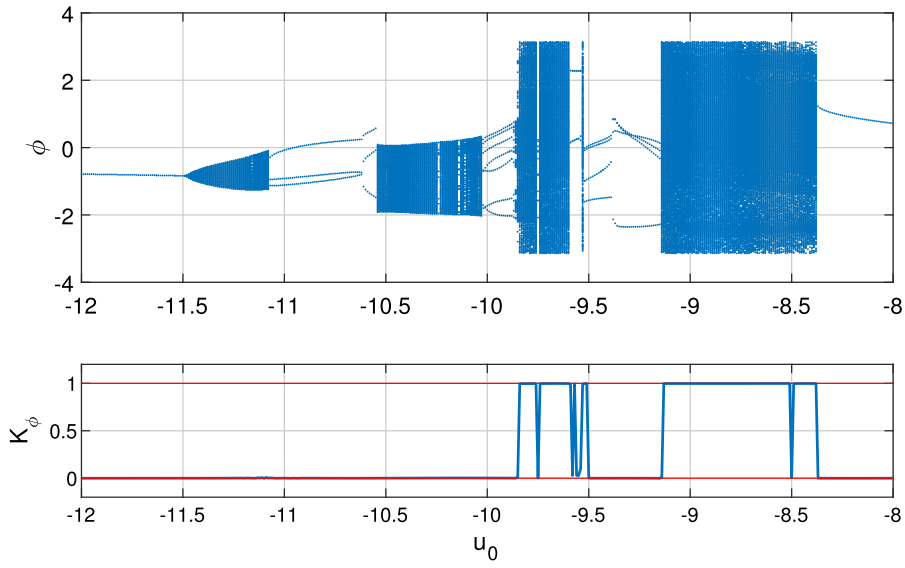

Fig. 7 Bifurcation diagram due to a quasistatic increase in the parameter value u_0 together with the $K = K_\phi$ values of the 0–1 test (estimated from Eq. 12)

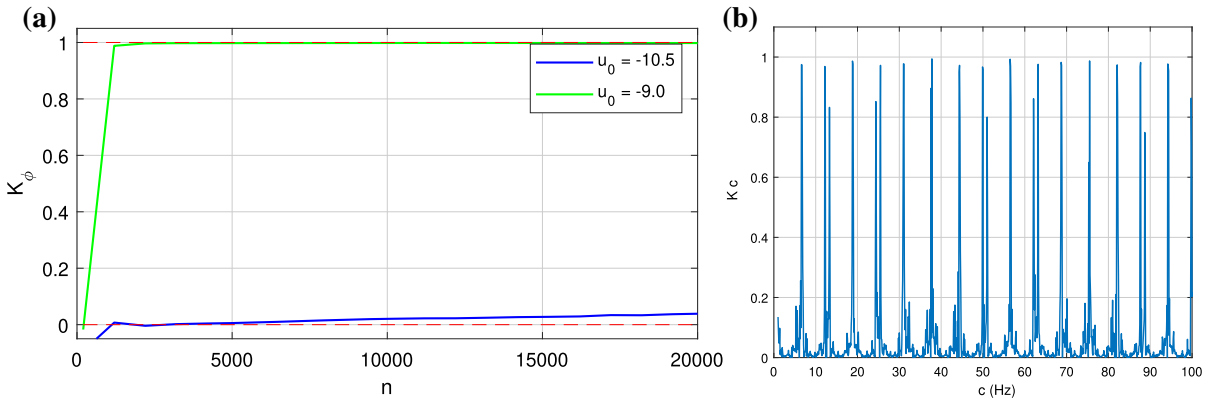

Fig. 8 (**a**) scaling of K_ϕ (for periodic with u_0=−10.5V and non-periodic with $u_0 = -9$ V response) depending on the length of the time series n (Eqs. 11, 12). (**b**) c dependence of Kc. One can see the resonances in particular for the case of $u_0 = -10.5$ V. To avoid the resonating condition in the variable transform (Eq. 9), we used averaging over c

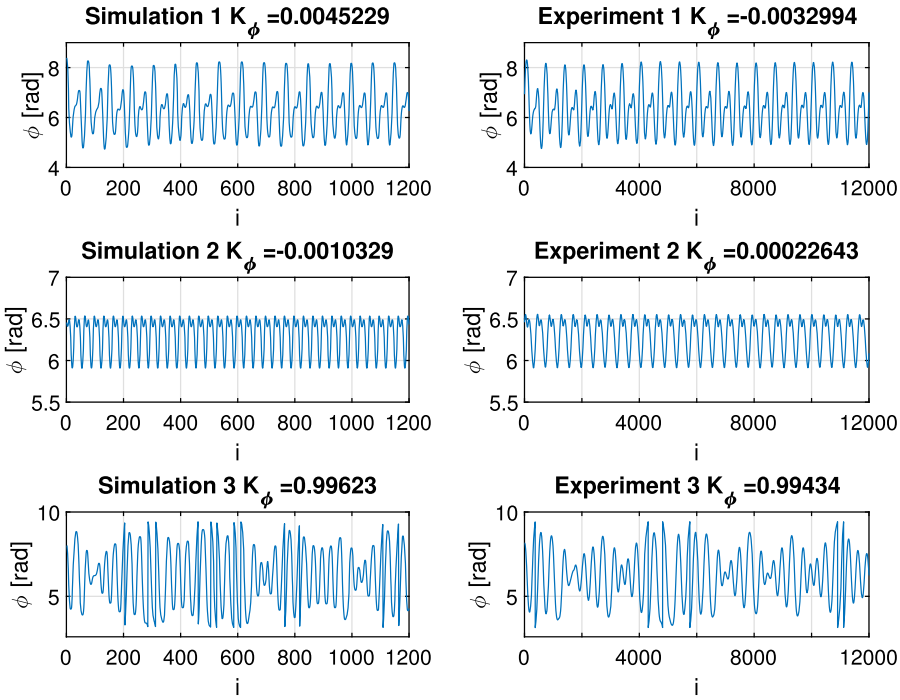

Fig. 9 Time series of ϕ coordinate for selected values u_0 for both simulations (left) and experiment (right) with corresponding values of the 0–1 test

cation diagram (Fig. 7) correspond to periodic solutions. Interestingly, the black areas in bifurcation diagrams correspond to both: quasi-periodic ($u_0 \in (-11.50, -11.05) \cup (-10.55, -10.05)$) and chaotic ($u_0 \in (-9.86, -9.51) \cup (-9.13, -8.38)$ solutions. This is identified by K values (0 or 1, respectively) and confirmed by the corresponding power spectra (Fig. 5) and phase portraits (Fig. 3). In these figures u_0=−11.25 and −10.2V lead to quasi-periodic solutions. Scaling of $K = K_\phi$ (for periodic with $u_0 = -10.5$V and non-periodic with $u_0 = -9$V response) depending on the length of the time series n and the corresponding dependence of K_c is presented in Fig. 8a, b. Note that the bifurcation diagram may slightly differ from the results of Fig. 4 (see the case of u_0=−11.75) because of different initial conditions.

Another qualitative test using the scale index was discussed by [31,32]. It could be used to distinguish

particular periodicities of solution from chaotic solutions.

As mentioned earlier, the analyzed pendulum system parameters were identified in [17]. To confirm the results of the 0–1 test, the selected time series obtained from the simulation as well as the experiment together with the values of the K function are shown in Fig. 9. Simulation and experiment no 1 correspond to input voltage $u_0 = -10.8$ V, no 2—$u_0 = -6.5$ and no 3—$u_0 = -8.51$. The first to experiments correspond to the solutions used during parameters' estimation. Note that the solutions presented in Fig. 9 are shifted by multiplicity of 2π, since during the ignored transient motions full rotations of the pendulum can occur. It can be noticed that also in the case of data obtained from the experiment, the $K \approx 0$ clearly identifies the periodic response of the system (Experiments 1 and 2), and the $K \approx 1$ clearly indicates the chaotic response of the system (Experiment 3).

5 Conclusions

The mathematical model of a pendulum with a peculiar periodic excitation (with higher harmonics) was verified based on the conducted experiment, which allowed to examine the sensitivity of the system to change the parameter u_0 and to observe different bifurcation scenarios like period doubling and inverse period doubling). The selected periodic, quasi-periodic and non-periodic solutions were observed in phase diagrams and Poincaré maps as well as confirmed by spectral analysis.

In the further part of the work, a nonlinear chaos identification method was proposed to confirm the obtained results in a quantitative way. The K function values clearly distinguished between regular and irregular vibrations, both in the case of numerical simulations as well as experimental results. The obtained results indicate that the chosen method of analysis turned out to be effective, and at the same time relatively easy to implement compared to other methods of nonlinear dynamics, e.g., the maximal Lyapunov exponent.

It should be noted that the pendulum driven by through a DC motor and slider–crank mechanism is rather rarely investigated with realistic models, taking into account details concerning motion resistances in the joints, realistic mass distribution etc. The reason of such a situation is rarity or lack of experimental investigations of such a type of systems. Therefore, as one of the achievements of the present work can be indicated the realistic modeling and very good agreement with the experimental data. It has allowed for original and positive tests of the 0–1 method for chaos detection with parallel investigations of real and numerical signals.

Acknowledgements This work has been supported by the Polish National Science Centre under the Grant OPUS 14 No. 2017/27/B/ST8/01330.

Compliance with ethical standards

Conflicts of interest The authors declare that they have no conflict of interest.

References

1. Blackburn, J.A., Zhou-Jing, Y., Vik, S., Smith, H.J.T., Nerenberg, M.A.H.: Experimental study of chaos in a driven pendulum. Phys. D **26**(1–3), 385–395 (1987)
2. Miles, J.: On resonant rotation of a weakly damped pendulum. J. Sound Vib. **280**(1–2), 401–406 (2005)
3. Baker, G.L., Gollub, J.P.: Chaotic Dynamics: An Introduction. Cambridge University Press, Cambridge (1996)
4. Baker, G.L., Blackburn, J.A.: The Pendulum. A Case Study in Physics. Oxford University Press, Oxford (2005)
5. Luo, A.C.J.: Resonance and Bifurcation to Chaos in Pendulum. World Scientific, Singapore (2018)
6. Litak, G., Wiercigroch, M., Horton, B.W., Xu, X.: Transient chaotic behaviour versus periodic motion of a parametric pendulum by recurrence plots. ZAMM - Z. Angew. Math. Mech. **90**(1), 33–41 (2010)
7. Kovaleva, M., Manevitch, L., Romeo, F.: Stationary and non-stationary oscillatory dynamics of the parametric pendulum. Commun. Nonlinear Sci. Numer. Simul. **76**(4), 1–11 (2019)
8. Dostal, L., Korner, K., Kreuzer, E., Yurchenko, D.: Pendulum energy converter excited by random loads. ZAMM-Z. Angew. Math. Mech. **98**(3), 349–366 (2018)
9. Awrejcewicz, J., Supeł, B., Kudra, G., Lamarque, C.-H., Wasilewski, G., Olejnik, P.: Numerical and experimental study of regular and chaotic motion of triple physical pendulum. Int. J. Bifurc. Chaos **18**(10), 2883–2915 (2008)
10. Rivas-Cambrero, I., Sausedo-Solorio, J.M.: Dynamics of the shift in resonance frequency in a triple pendulum. Meccanica **47**(4), 835–844 (2012)
11. Awrejcewicz, J., Wasilewski, G., Kudra, G., Reshmin, S.A.: An experiment with swinging up a double pendulum using feedback control. J. Comput. Syst. Sci. **51**(2), 176–182 (2012)
12. Alevras, P., Brown, I., Yurchenko, D.: Experimental investigation of a rotating parametric pendulum. Nonlinear Dyn. **81**, 201–213 (2015)
13. Yurchenko, D., Alevras, P.: Parametric pendulum based wave energy converter. Mech. Syst. Signal Process. **99**, 504–515 (2018)

14. Belato, D., Weber, H.I., Balthazar, J.M., Mook, D.T.: Chaotic vibrations of a nonideal electromechanical system. Int. J. Solids Struct. **38**, 1699–1706 (2001)
15. Kaźmierczak, M., Kudra, G., Awrejcewicz, J., Wasilewski, G.: Numerical and experimental investigations of bifurcational dynamics of an electromechanical system consisting of a physical pendulum and DC motor. In: Awrejcewicz, J., Kaźmierczak, M., Olejnik, P., Mrozowski, J. (eds.) Dynamical Systems-Applications, pp. 49–58. TU of Lodz Press, Lodz (2013)
16. Kaźmierczak, M., Kudra, G., Awrejcewicz, J., Wasilewski, G.: Mathematical modelling numerical simulations and experimental verification of bifurcation dynamics of a pendulum driven by a DC motor. Eur. J. Phys. **36**(055028), 1–13 (2015)
17. Wasilewski, G., Kudra, G., Awrejcewicz, J., Kaźmierczak, M., Tyborowski, M., Kaźmierczak, M.: A pendulum driven by a crank-shaft-slider mechanism and a DC motor—mathematical modelling, parameter identification and experimental validation of bifurcational dynamics. In: Awrejcewicz, J. (ed.) Springer Proceedings in Mathematics and Statistics-Dynamical Systems: Theoretical and Experimental Analysis, pp. 385–398. Springer, Cham (2016)
18. Avanço, R.H., Navarro, H.A., Brasil, R.M., Balthazar, J.M., Bueno, Á.M., Tusset, A.M.: Statements on nonlinear dynamics behavior of a pendulum, excited by a crank-shaft-slider mechanism. Meccanica **51**, 1301–1320 (2016)
19. Avanço, R.H., Tusset, A.M., Suetake, M., Navarro, H.A., Balthazar, J.M., Nabarrete, A.: Energy harvesting through pendulum motion and DC generators. Lat. Am. J. Solids Struct. **16**(1), e150 (2019)
20. Felix, L.P., Balthazar, J.M.: Comments on a nonlinear and nonideal electromechanical damping vibration absorber, Sommerfeld effect and energy transfer. Nonlinear Dyn. **55**(1–2), 1–11 (2009)
21. Cveticanin, L.: Dynamics of the non-ideal mechanical systems: a review. J. Serbian Soc. Comput. Mech. **4**(2), 75–86 (2010)
22. Samantaray, A.K., Dasgupta, S.S., Bhattacharyya, R.: Sommerfeld effect in rotationally symmetric planar dynamical systems. Int. J. Eng. Sci. **48**, 21–26 (2010)
23. Bernardini, D., Litak, G.: An overview of 0–1 test for chaos. J. Braz. Soc. Mech. Sci. Eng. **38**, 1433–1450 (2015)
24. Nelder, J.A., Mead, R.: A simplex method for function minimization. Comput. J. **7**(4), 308–313 (1965)
25. Gershenfeld, N.: The Nature of Mathematical Modelling. Cambridge University Press, Cambridge (2011)
26. Wood, S.N.: Minimising model fitting objectives that contain spurious local minima by bootstrap restarting. Biometrics **57**, 240–244 (2001)
27. Gottwald, G.A., Melbourne, I.: On the implementation of the 0–1 test for chaos. SIAM J. Appl. Dyn. Syst. **8**, 129–145 (2009)
28. Syta, A., Litak, G., Lenci, S., Scheffler, M.: Chaotic vibrations of the duffing system with fractional damping. Chaos **24**, 013107 (2014)
29. Gottwald, G.A., Melbourne, I.: Chaos Detection and Predictability, pp. 221–247. Springer, Berlin (2016)
30. Syta, A., Bowen, C.R., Kim, H.A., Rysak, A., Litak, G.: Experimental analysis of the dynamical response of energy harvesting devices based on bistable laminated plates. Meccanica **50**, 1961–1970 (2015)
31. Benitez, R., Bolós, V.J., Ramirez, M.E.: A wavelet-based tool for studying non-periodicity. Comput. Math. Appl. **60**, 634–641 (2010)
32. Tusset, A.M., Santo, D.R., Balthazar, J.M., Piccirillo, V., Santos, L.C.C.D., Brasil, R.M.: Active vibration control of an elevator system using magnetorheological damper actuator. Int. J. Nonlinear Dyn. Control **1**, 114–131 (2017)